

A bandwidth-optimized WENO scheme for the effective direct numerical simulation of compressible turbulence

M.P. Martín ^{a,*}, E.M. Taylor ^a, M. Wu ^a, V.G. Weirs ^b

^a *Department of Mechanical and Aerospace Engineering, Princeton University,
Princeton, NJ 08544, United States*

^b *Sandia National Laboratories, Albuquerque, NM, United States*

Received 12 October 2005; received in revised form 4 April 2006; accepted 10 May 2006
Available online 12 July 2006

Abstract

Two new formulations of a symmetric WENO method for the direct numerical simulation of compressible turbulence are presented. The schemes are designed to maximize order of accuracy and bandwidth, while minimizing dissipation. The formulations and the corresponding coefficients are introduced. Numerical solutions to canonical flow problems are used to determine the dissipation and bandwidth properties of the numerical schemes. In addition, the suitability and accuracy of the bandwidth-optimized schemes for direct numerical simulations of turbulent flows is assessed in decaying isotropic turbulence and supersonic turbulent boundary layers.

© 2006 Elsevier Inc. All rights reserved.

Keywords: Direct numerical simulation; Shock capturing; Bandwidth optimization; Turbulence; Compressible flow

1. Introduction

The detailed simulation of compressible turbulent flows requires solving the conservation of mass, momentum and energy equations. For direct numerical simulations (DNS) all possible turbulent length scales and time scales must be resolved by the numerical method. Thus, DNS requires accurate representation of time-dependent propagation of high wavenumber (or high frequency), small amplitude waves. In addition, compressible turbulent flows are characterized by shockwaves that result in a sudden change of the fluid properties. Therefore, methods for compressible turbulent flows require robust shock capturing, as well as minimal dissipation and dispersion errors.

Resolving the shock thickness is impractical for the detailed simulation of turbulence, as the mean free path is typically orders of magnitude smaller than that of the Kolmogorov length scale [1,2]. In the present simulations, we resolve all turbulent length scales and time scales, while shocks are not being resolved. In turn, the simulations within are “effective” direct numerical simulations.

* Corresponding author. Tel.: +1 609 258 7318; fax: +1 609 258 1993.
E-mail address: pmartin@princeton.edu (M.P. Martín).

Fig. 1 shows a numerical schlieren image from a DNS of a shock and turbulent boundary layer interaction at Mach 3 and Reynolds number based on momentum thickness $Re_\theta = 2400$ [3,4]. In this flow, a turbulent boundary layer is convected over a 24° compression ramp, which generates a shockwave. The turbulent structures in the incoming boundary layer are apparent. The unsteady nature of the boundary layer causes the shock to wrinkle and oscillate near the corner. Downstream of the corner, the boundary layer remains compressed between the wall and the compression-corner shock, and additional shocks emanate from the large structures in the wake of the boundary layer and merge with the compression-corner shock while convecting downstream. Computing all the relevant turbulence structures in this flow requires high order of accuracy and bandwidth-resolving efficiency, as well as shock capturing for the unsteady shockwaves. Weighted essentially non-oscillatory (WENO) schemes provide a means for the DNS of compressible turbulent flow.

In WENO schemes [5], the numerical flux is computed as the weighted sum of a set of candidate flux approximations. The weights depend dynamically on the local smoothness of the data. Smoothness measurements cause stencils that span large flow field gradients to be assigned small relative weights; any candidate stencil containing a shock receives a nearly zero weight. In completely smooth regions, weights revert to optimal values, where optimal is defined by, e.g. maximum order of accuracy or maximum bandwidth. This weighting procedure makes the WENO schemes more robust than their predecessors, the essentially non-oscillatory (ENO) schemes (see for example [6,7]), which use the single smoothest candidate stencil to the exclusion of the others.

Jiang and Shu [8] cast WENO into finite-difference form and provide an efficient numerical implementation of the shock-capturing technique so that conditional statements are avoided. This scheme, which is referred as WENO-JS hereafter, provides robust shock-capturing, high-order accuracy and efficient implementation on distributed memory, multiprocessor machines. However, WENO-JS is too dissipative for the detailed simulation of turbulent flow.

There have been a number of efforts to overcome the deficiencies of conventional shock-capturing schemes for the detailed simulation of compressible turbulence. Adams and Shariff [9] developed a hybrid scheme that couples compact upwind and shock-capturing ENO schemes, in which the ENO scheme is activated only around discontinuities. Pirozzoli [10] follows a similar approach and replaces the non-conservative formulation of the compact scheme with a conservative one and the ENO with WENO, resulting in a more stable and accurate algorithm. Ren et al. [11] improve the hybrid compact-WENO scheme [10] by removing the abrupt switch between the compact and the shock-capturing schemes through the use of a weighted average of the two schemes. Hill and Pullin [12] use a version in which the non-shock-capturing scheme is centered rather than upwind-biased, thereby reducing the overall dissipation in smooth flow regions. Kim and Kwon [13] propose an additional formulation of a hybrid central-difference WENO scheme with an alternative weighting function for the two schemes.

Rather than combining two different schemes and choosing when to use each one, in this paper we apply a modified version of Jiang and Shu's method everywhere in the flowfield. The purpose of the non-linear adaptation mechanism in WENO schemes is choosing when to use the optimal stencil and when to use a smaller stencil to avoid interpolation across high gradients (which result in numerical oscillations). Thus, there are two sources of WENO dissipation: that associated with the adaptation mechanism and that of the optimal stencil.

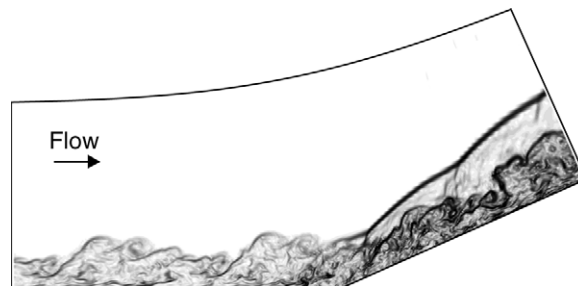


Fig. 1. Numerical schlieren from the DNS of a shockwave/turbulent boundary layer interaction. The incoming boundary layer is at Mach 3 and $Re_\theta = 2400$ [3,4].

Here, we focus on reducing the dissipation of the optimal stencil and assess the resulting scheme for the detailed simulation of compressible turbulence. Wang and Chen [14] perform a similar study where they optimize the candidate and optimal stencils of Jiang and Shu upwind biased WENO schemes, while minimizing the error in wavenumber space and applying the schemes to linear problems.

The modifications that we make to Jiang and Shu’s scheme are to (i) add an additional candidate stencil so that the set of candidates is symmetric, rather than upwind-biased, and (ii) use bandwidth optimization to determine the weights for the optimal stencil, maintaining a small amount of dissipation at high wavenumbers. The essential idea of bandwidth optimization is to minimize the truncation error on a given grid. In traditional order optimization, the goal is to minimize the error most rapidly as the grid is refined. Ultimately, we choose to specify constraints from each type of optimization.

Thus in this paper, we present bandwidth-optimized WENO schemes for the direct numerical simulation of turbulent compressible flows. In Sections 2 and 3, we briefly describe the WENO-JS scheme and the concept of bandwidth for a numerical scheme. In Section 4, we present bandwidth-optimized WENO schemes that are suitable for DNS of turbulence. In Section 5.5, we assess and validate the schemes in canonical test problems and in Sections 6 and 7, we use the new schemes in DNS of compressible isotropic turbulence and turbulent boundary layers. We present the conclusions in Section 8.

2. WENO method of Jiang and Shu

We describe the WENO method of Jiang and Shu [8] in the context of the scalar, one-dimensional advection equation,

$$\frac{\partial u}{\partial t} + \frac{\partial}{\partial x} f(u) = 0. \tag{1}$$

This model equation represents the decoupled forms of equations belonging to any system of hyperbolic conservation laws after they are transformed from physical into characteristic space. If the spatial domain is discretized such that $x_i = i\Delta$, where Δ is the grid spacing, and \hat{u}_i is the numerical approximation to $u(x_i)$, Eq. (1) may be cast into the semidiscretized form

$$\frac{d\hat{u}_i}{dt} = -\frac{1}{\Delta} \left(\hat{f}_{i+\frac{1}{2}} - \hat{f}_{i-\frac{1}{2}} \right), \tag{2}$$

where $\hat{f}_{i+1/2}$ is a numerical approximation of $f(u(x_{i+1/2}))$. Once the right-hand side of this expression has been evaluated, numerical techniques for solving ordinary differential equations, such as Runge–Kutta methods, may be employed to advance the solution in time. To ensure stability, $f(u)$ is generally split into $f^+(u)$, which has a strictly non-negative derivative, and $f^-(u)$, which has a strictly non-positive one.

WENO schemes compute $\hat{f}_{i+1/2}^+$ through interpolating polynomials on a number of overlapping candidate stencils, each containing r grid points. In the WENO-JS method, there are r candidate stencils. The one most upwinded candidate stencil ranges over mesh point indices $(i - r + 1)$ to i , the fully downwinded candidate stencil ranges over i to $(i + r - 1)$, and the other candidate stencils fall in between. Fig. 2 provides a schematic of this arrangement. Note that this collection of stencils is not symmetric about the point $(i + \frac{1}{2})$, and thus the final combination is likely to be biased toward the upwind direction.

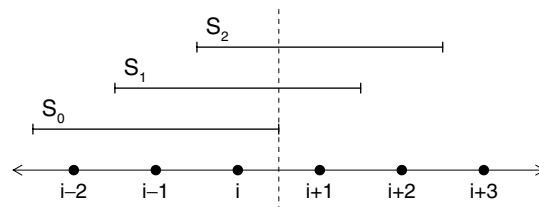


Fig. 2. Candidate stencils S_k for the numerical flux $\hat{f}_{i+1/2}^+$ when $r = 3$ in the WENO-JS method.

If the flux approximation on stencil k , which contains r grid points, is designated q_k^r and the weight assigned to that stencil is ω_k , the final numerical approximation becomes

$$\hat{f}_{i+\frac{1}{2}}^+ = \sum_{k=0}^{r-1} \omega_k q_k^r. \tag{3}$$

Specifically, q_k^r are r th-order accurate polynomial interpolants evaluated at $x_{i+1/2}$, computed by

$$q_k^r|_{i+\frac{1}{2}} = \sum_{l=0}^{r-1} a_{kl}^r f(u_{i-r+k+l+1}), \tag{4}$$

where a_{kl}^r are the stencil coefficients. The weights are defined by

$$\alpha_k = \frac{C_k^r}{(\varepsilon + \text{IS}_k)^p} \tag{5}$$

and

$$\omega_k = \frac{\alpha_k}{\sum_{k=0}^{r-1} \alpha_k}. \tag{6}$$

The constant ε prevents division by zero, and p may be varied to increase or decrease WENO adaptation sensitivity. The smoothness measurement IS_k becomes large when discontinuities are present within stencil k and remains relatively small otherwise. When $r \leq 4$, the strict definition of IS_k as presented by Jiang and Shu [8] may be expressed in the “nice” form

$$\text{IS}_k = \sum_{m=1}^{r-1} \left(\sum_{l=0}^{r-1} a_{kml}^r f(u_{i-r+k+l+1}) \right)^2, \tag{7}$$

where d_{kml}^r are additional tabulated coefficients. In completely smooth regions, each candidate stencil is equally desirable, and ω_k revert to the optimal weights C_k^r .

The corresponding stencil diagram for $\hat{f}_{i+1/2}^-$ is simply a mirror image of Fig. 2. The total number of grid points available to the WENO-JS numerical flux in Eq. (3) is $(2r - 1)$. Consequently the maximum order of accuracy of the WENO-JS algorithm is $(2r - 1)$. The order-optimized optimal weights C_k^3 and C_k^4 as well as the coefficients a_{kl}^3 , a_{kl}^4 , d_{kml}^3 , and d_{kml}^4 are tabulated in Appendix.

3. Bandwidth properties of a numerical scheme

Bandwidth-resolving efficiency is a measure of the frequency resolution achieved by a numerical scheme and is therefore important for the detailed simulation of turbulence, in which relevant length scales span several orders of magnitude. The computational grid itself contributes to bandwidth properties: the largest resolvable wavelength is equal to the length of the domain, and the smallest is equal to two grid spacings. The latter, however, is a theoretical limit because numerical methods may impose additional constraints. Though spectral methods are designed to fully resolve all available wavenumbers, their global operations render them inefficient for parallel computing. Alternatively, finite-difference schemes, which are local in nature and thus minimize interprocessor communication, cannot capture the highest wavenumbers supported by the grid. WENO methods belong to the second class.

The bandwidth properties of linear numerical schemes are determined by Fourier analysis. Consider a pure harmonic function

$$f(x) = e^{ikx}, \tag{8}$$

in which x is position and k is wavenumber. Then

$$f'(x) = ikf(x) \tag{9}$$

and, if we define n as any integer and Δ as grid spacing,

$$f(x + n\Delta) = e^{ink\Delta} f(x). \tag{10}$$

A general finite-difference method approximates the first derivative f' according to the formula

$$\tilde{f}'(x) = \frac{1}{\Delta} \sum_n a_n f(x + n\Delta), \tag{11}$$

in which a_n are non-dimensional stencil coefficients which uniquely define the particular scheme. (The tilde indicates that this numerical derivative is equivalent to the analytic derivative of some close but unknown function \tilde{f} .) We may equate Eqs. (9) and (11) to yield

$$i\tilde{k}f(x) = \frac{1}{\Delta} \sum_n a_n e^{ink\Delta} f(x). \tag{12}$$

If we define the scaled wavenumber κ by $\kappa = k\Delta$, Eq. (12) reduces to

$$\tilde{\kappa} = -i \sum_n a_n e^{in\kappa}, \tag{13}$$

where $\tilde{\kappa}$ is known as the modified wavenumber; through the a_n coefficients, which define the finite difference scheme, $\tilde{\kappa}$ is the numerical approximation to κ . A numerical method that fully resolved all wavenumbers would produce $\tilde{\kappa} = \kappa$ for $0 \leq \kappa \leq \pi$.

Fig. 3 presents $\tilde{\kappa}(\kappa)$ for various finite-difference methods. Above $\tilde{\kappa} = 0$ are the real parts, which describe phase errors, and below are the imaginary parts, which describe dissipative amplitude errors. For example, the first-order backward and second-order central difference schemes have identical phase-error characteristics, but the backward difference scheme generates significant dissipation while the central scheme produces none. One approach to optimizing bandwidth properties is to delay the separation of the real part of $\tilde{\kappa}$ from $\tilde{\kappa} = \kappa$ to the highest feasible wavenumber. For such a process Lele [15] defines phase error as $(\tilde{\kappa} - \kappa)/\kappa$ and bandwidth-resolving efficiency index as the value of κ/π for which this error first rises above an arbitrary threshold ε . The sixth-order accurate Padé scheme, which is included in Fig. 3, was designed using this approach [15] and is commonly used for the DNS of shock-free turbulent flows. A second and often interwoven approach to optimizing bandwidth properties is to shift dissipation errors to those wavenumbers for which the phase errors are already considerable. This allows small amounts of deliberate dissipation to continue to stabilize a simulation without corrupting the well-resolved part of the spectrum.

The optimal weights define a linear numerical scheme; this scheme can be analyzed to determine its bandwidth properties with Fourier analysis. The optimal weights specify the upper bound of WENO bandwidth performance, which is achieved when the adaptation mechanism is switched off. Fig. 4 plots $\tilde{\kappa}(\kappa)$ for the WENO-JS optimal stencil when $r = 3$ and $r = 4$ as well as for the sixth-order Padé scheme. When ε is set to 0.01, Lele’s bandwidth-resolving efficiency index is 0.35 for $r = 3$ and 0.42 for $r = 4$. In order to restrict dis-

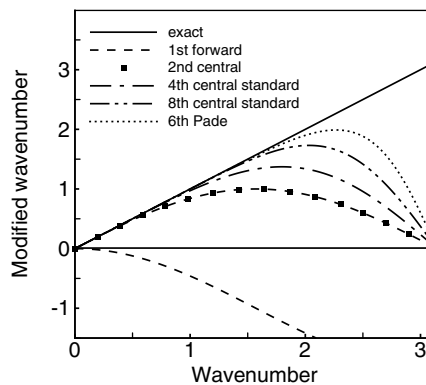


Fig. 3. Bandwidth efficiency for several numerical schemes.

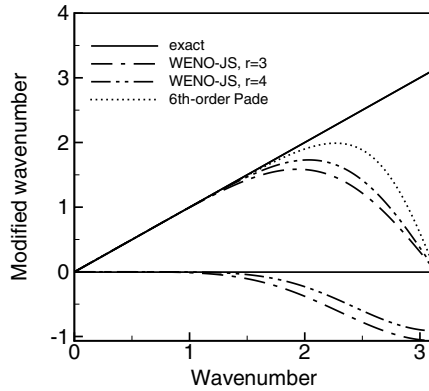


Fig. 4. Bandwidth efficiency for WENO-JS.

sipation to wavenumbers for which phase errors are greater than the more lenient threshold of 20%, amplitude errors should be negligible for $\kappa < 2$. Quantifying amplitude errors as precisely as phase errors is difficult because ideal dissipation is zero everywhere, but visual inspection of Fig. 4 suggests that the WENO-JS method does not satisfy this condition.

4. Bandwidth-optimized WENO method

The bandwidth-optimized WENO method [16] modifies the WENO-JS method according to two distinct strategies. Recall that the second-order central scheme described in Fig. 3, unlike the related first-order backward scheme, exhibited zero amplitude errors; this is typical of central numerical methods. Also consider the observation in Section 2 that the center of the stencil collection represented by Fig. 2 lies slightly upwind of the point $(i + \frac{1}{2})$. If an additional candidate stencil were available downwind of that point, the collection would be symmetric, and thus the optimal weights would be theoretically capable of providing zero dissipation. This constitutes the first modification, which we call WENO-SYM, and Fig. 5 depicts the new candidate stencil arrangement for $r = 3$.

Including an extra candidate stencil changes only a few of the equations of Section 2. The final flux approximation of Eq. (3) becomes

$$\hat{f}_{i+\frac{1}{2}}^+ = \sum_{k=0}^r \omega_k q_k^r, \tag{14}$$

while the particular values of the coefficients a_{kl}^r and d_{kml}^r , remain unaffected. Because stencil r contains purely downwind information, preferential weighting of that stencil at the expense of the others could cause instabilities. Therefore, after the smoothness measurements IS_k are computed via Eq. (7), IS_r is further constrained to satisfy

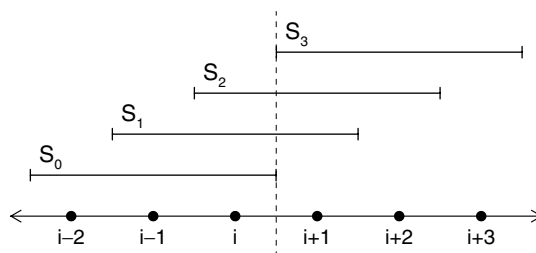


Fig. 5. Candidate stencils S_k for the numerical flux $\hat{f}_{i+\frac{1}{2}}^+$ when $r = 3$ in the WENO-SYM method.

$$\text{IS}_r = \max_{0 \leq k \leq r} \text{IS}_k. \quad (15)$$

This ensures that the normalized weight ω_r can be no larger than the least of all ω_k .

Since the total number of grid points available for the calculation of $f_{i+1/2}^+$ has increased, the optimal weights of the WENO-SYM method differ from those of the WENO-JS method. The WENO-SYM order-optimized optimal weights \bar{C}_k^r can now provide $2r$ th-order of accuracy as opposed to $(2r - 1)$ th-order, and we designate this scheme WENO-SYMOO. These optimal weights result in an optimal stencil with no numerical dissipation; the \bar{C}_k^3 and \bar{C}_k^4 are listed in Appendix.

On the other hand, one may design bandwidth-optimized optimal weights \tilde{C}_k^r that maximize Lele's bandwidth-resolving efficiency index, and we refer to this scheme as WENO-SYMOB. This bandwidth optimization technique constitutes the second modification of the WENO-JS method, and details about the process may be found in [16–18]. Namely, the bandwidth optimization is expressed as the minimization of an integrated error function. Following [16], the error function used is

$$I = \int_0^\pi e^{v(\pi-\kappa)} \left(\sigma [\Re(\kappa') - \kappa]^2 + (1 - \sigma) [\Im(\kappa') - \gamma \sin^\mu(\kappa/2)]^2 \right) d\kappa. \quad (16)$$

In this function, the optimal weights embedded in κ' are the free parameters. We have chosen to define the stencil coefficients a_{kl}^r , also embedded in the modified wavenumber, completely through the order of accuracy constraints. In so doing, we specify the resulting schemes will be r th-order accurate.

Recall the phase errors are associated with the real part of the modified wavenumber $\Re(\kappa')$, and the amplitude errors with the imaginary part $\Im(\kappa')$; $\sigma = 1/2$ specifies each type has equal importance. The sine term is used to add a dissipative bias ($\gamma = -1$) to the optimal weights, particularly at high wavenumbers as specified by $\mu = 16$. Finally the exponential term heavily weights the error at the lower end of the spectrum; we chose $v = 6$ for the $r = 3$ weights, and $v = 8$ for $r = 4$. As finite difference schemes cannot resolve the highest wavenumbers, the errors for these wavenumbers are deemphasized in the minimization procedure.

The error function and the parameters (σ , μ , v and γ) we have used were developed by trial and error. Ultimately, the bandwidth-optimized optimal weights we “derived” are subjective, but not arbitrary. Regarding the phase error, the optimization parameters were chosen to extend the well-resolved part of the spectrum while maintaining essentially the same accuracy as the order-optimized weights at low wavenumbers. Regarding the truncation error terms of the optimal stencil, the optimization affected only the higher order terms. (This is achieved by retaining the order-optimized candidate stencil coefficients a_{kl}^r .) The amount of dissipation added was subjectively chosen, but is much less than the WENO-JS scheme, and could be reduced or eliminated entirely if stability were not an issue.

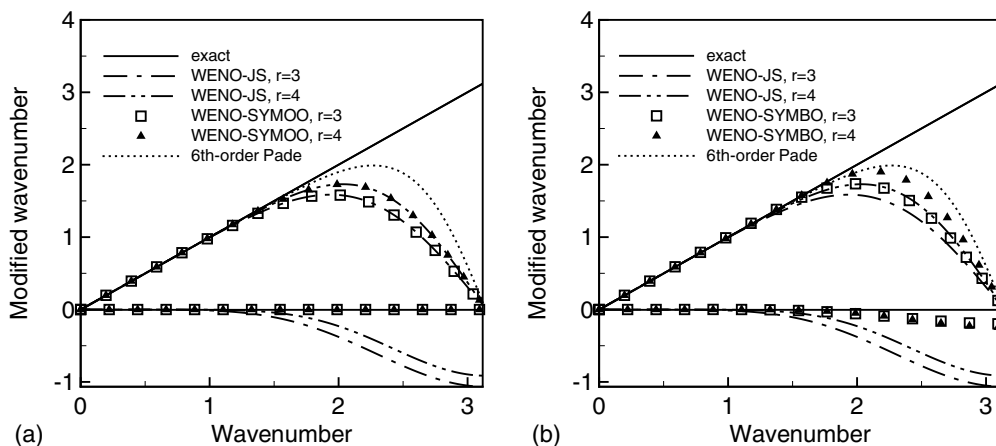


Fig. 6. Bandwidth efficiency for the (a) WENO-SYMOO and (b) WENO-SYMOB optimal stencils in comparison with the WENO-JS optimal stencil and a sixth-order accurate Padé scheme.

Mathematica [19] was used to perform the minimization and determine \tilde{C}_k^3 , and \tilde{C}_k^4 , which are listed in Appendix. Fig. 6 displays the bandwidth properties for the WENO-SYMOO and WENO-SYMO optimal stencils as well as that for the original WENO-JS. Though the new order-optimized scheme takes maximum advantage of the symmetric stencil collection to generate zero amplitude errors, its phase errors are not improved. Only bandwidth-optimized optimal weights can accomplish the latter goal. The bandwidth-resolving efficiency index of the WENO-SYMO scheme is 0.49 (compared to 0.35) for $r = 3$ and 0.56 (compared to 0.42) for $r = 4$.

Note that we have modified the linear part of the weighted ENO scheme, the optimal stencil, which is used only when all the candidate stencils have equally smooth data. The non-linear part of the scheme, the adaptation mechanism, is also a source of numerical dissipation, which has not been optimized here.

5. Canonical test problems

In this section, we assess the WENO-SYM schemes and compare them to WENO-JS in problems without turbulence. For all the test cases presented here, a third-order Runge–Kutta scheme is used to advance the solution in time. For all simulations and schemes $\epsilon = 1.0 \times 10^{-10}$ and $p = 1$, unless indicated otherwise. It should be noted that the original WENO-JS formulation employs $p = 2$, which is a more dissipative choice than $p = 1$.

5.1. Propagation of a smooth disturbance

To assess the dissipation of the bandwidth-optimized scheme relative to that of the original WENO-JS scheme, we consider the propagation of a linear one-dimensional disturbance. The governing equation is the linear advection equation, Eq. (1), with $f(u) = u$. Namely,

$$\frac{\partial u}{\partial t} + \frac{\partial u}{\partial x} = 0. \tag{17}$$

We initialize the disturbance at $t = 0$ with a sine wave

$$u(x) = \sin\left(\frac{2\pi x}{a\Delta}\right), \tag{18}$$

where $a\Delta$ is the wavelength of the disturbance and a represents the number of grid points per wavelength (PPW). We use two tests with 16 and 8 PPW, which correspond to $\kappa = 0.393$ and 0.785, respectively.

Fig. 7 shows the solution given by the different WENO schemes after the waveform has propagated one wavelength. In Fig. 7(a) for 16 PPW, all WENO schemes represent the exact solution accurately. As we coarsen the grid to 8 PPW, Fig. 7(b), the amplitude of the wave relative to the exact solution is reduced by the

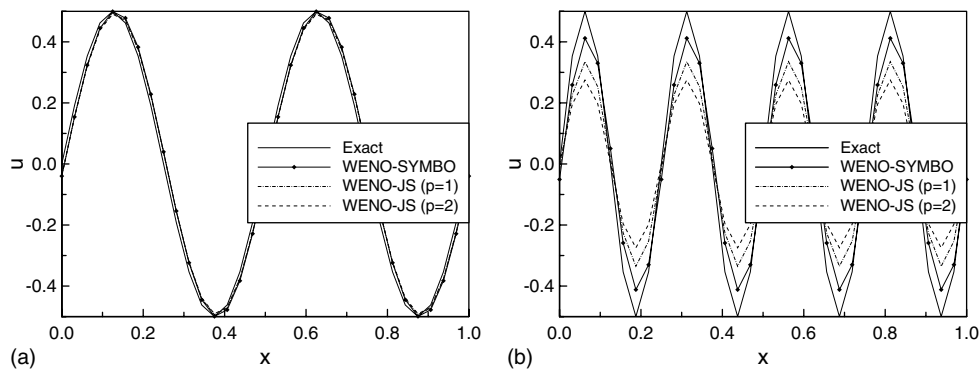


Fig. 7. Solution to the one-dimensional wave equation with (a) 16 PPW and (b) 8 PPW.

numerical dissipation. The WENO-SYMO is the least dissipative WENO scheme, followed by WENO-JS with $p = 1$ and the original WENO-JS with $p = 2$.

5.2. Shock tube problem

Fluid motion through a shock tube requires the resolution of shockwaves and expansion waves in laminar flow. The flow is one-dimensional and inviscid. The governing equations are the inviscid Navier–Stokes equations, or Euler equations, which can be written in conservation form as

$$\begin{aligned} \frac{\partial \rho}{\partial t} + \frac{\partial}{\partial x}(\rho u) &= 0, \\ \frac{\partial(\rho u)}{\partial t} + \frac{\partial}{\partial x}(\rho u^2 + P) &= 0, \\ \frac{\partial E}{\partial t} + \frac{\partial}{\partial x}[(E + P)u] &= 0, \end{aligned} \quad (19)$$

where ρ is the density and u is the fluid velocity; $E = \frac{1}{2}\rho u^2 + \rho c_v T$ is the total energy per unit volume, where c_v is the constant-volume specific heat and T is the gas temperature; and P is the pressure. The ideal gas law, $P = \rho R T$ relates the thermodynamic variables and R is the gas constant.

In the initial flow configuration, a diaphragm separates a low-pressure (expansion) chamber from the high-pressure (compression) chamber. The basic governing parameter of the shock tube is the pressure ratio P_4/P_1 . The two chambers may be at different temperatures T_1 and T_4 , where subscripts 1 and 4 correspond to the low-pressure and high-pressure conditions, and might contain different gases with constants R_1 and R_4 . The diaphragm ruptures at $t = 0$. For $t > 0$, a shock propagates into the expansion chamber with speed u_s , and an expansion wave propagates into the compression chamber with finite speed a_4 at its front. Thus there is the region where the fluid has been traversed by the shock and that of the fluid traversed by the expansion wave. The interface between these two regions is a contact surface, also known as contact discontinuity, that marks the boundary between the fluids which were initially on either side of the diaphragm.

We consider the following conditions: $P_4/P_1 = 2$, $T_4/T_1 = 1$ and $R_4/R_1 = 1$. The diaphragm is located at $x/L = 0.5$, where L is the length of the shocktube, and we use 224 equispaced grid points. Figs. 8 and 9 plot the solution at time $t = 0.3L/a_0$ for $r = 3$ and $r = 4$, respectively. Pressure and density are shown to identify the different regions within the shocktube. For $r = 3$, all WENOs give accurate results. For $r = 4$, WENO-JS with $p = 2$ and WENO-SYMO give accurate results, whereas WENO-JS with $p = 1$ and WENO-SYMOO exhibit dispersive errors in the density profile.

5.3. Shu–Osher’s problem

This test problem includes the propagation of a Mach 3 (where the Mach number is the fluid velocity over the speed of sound) shockwave over smooth density fluctuations and was first proposed by Shu and Osher [7].

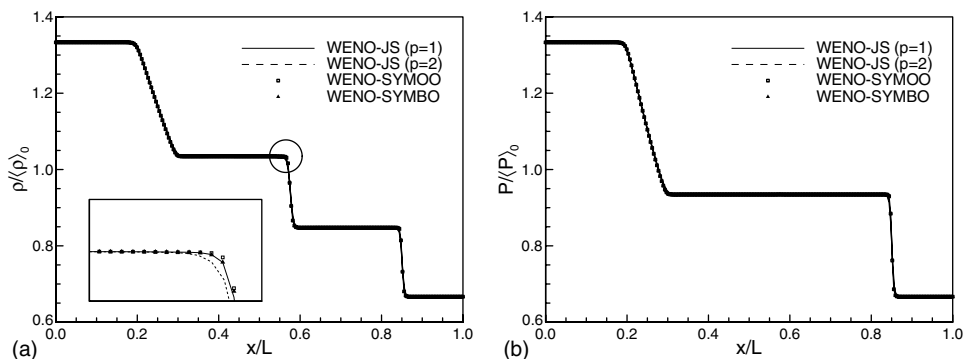


Fig. 8. Solution to a shock tube problem for the Euler equations for various WENO schemes with $r = 3$. (a) Density and (b) pressure normalized using initial values.

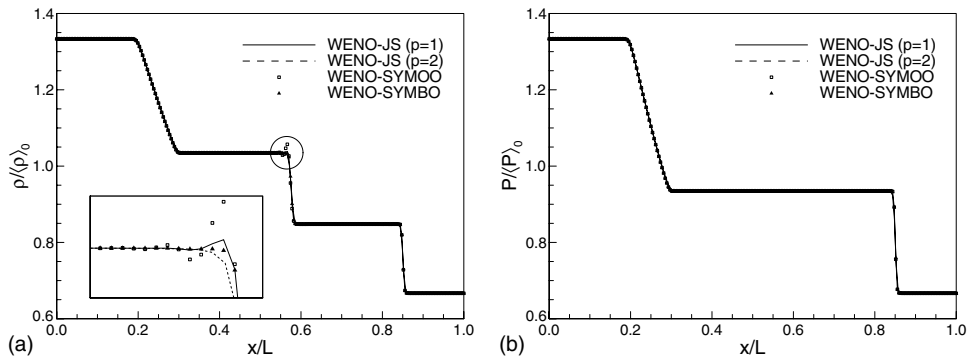


Fig. 9. Solution to a shock tube problem for the Euler equations for various WENO schemes with $r = 4$. (a) Density and (b) pressure normalized using initial values.

The initial non-dimensional flow conditions are $u = 0$, $p = 1$, and $\rho = 1 + 0.2\sin(5x)$ for $x \geq -4$; for $x < -4$, $u = 2.629369$, $p = 10.33333$ and $\rho = 3.857143$. In this test problem, small scale features follow the shockwave as it propagates from left to right. Resolving these structures is a good test of the bandwidth efficiency of a shock-capturing scheme. The governing equations are Eqs. (20).

The solution is advanced to $t = 1.8$. The CFL number is 0.2, which is low enough to ensure that time-advancement errors are dominated by spatial discretization errors. The grid is equispaced. The initial conditions are fixed at the boundaries for the duration of each simulation. The exact solution to Shu–Osher’s problem is not known. However, grid converged solutions are obtainable and serve as exact solutions. The reference solution here was computed by the unmodified WENO-JS scheme with $r = 3$ and $p = 2$ on 1600 grid points. Fig. 10(a) shows the computed density. The pressure is also shown in Fig. 10(b) as a reference for identifying the shock locations. At $t = 1.8$, the shock is at $x \approx 2.5$. To the right of the shock is the undisturbed, sinusoidal density field. To the left of the shock are physically correct oscillations at two different frequencies. Oscillations at the higher frequency follow immediately behind the shock, while oscillations at the same frequency as the initial density fluctuations extend a greater distance behind the shock. That is, an additional high-frequency component has been added by the passage through the shock. For the exact solution, even the high-frequency oscillations are resolved at approximately 60 points per wavelength. In the pressure profile the shock and trailing low-frequency oscillations are clearly discernible, but the high-frequency oscillations are confined to the density profile. To evaluate the bandwidth-resolving efficiency for the numerical schemes, we will only plot density profiles.

The solutions are presented for a fine grid (400 points) and a coarse grid (200 points). For consistency with the reference solution, all schemes use $p = 2$. The high-frequency oscillations farthest from the shock are examined closely, because these structures are formed at early t and have accumulated the most numerical

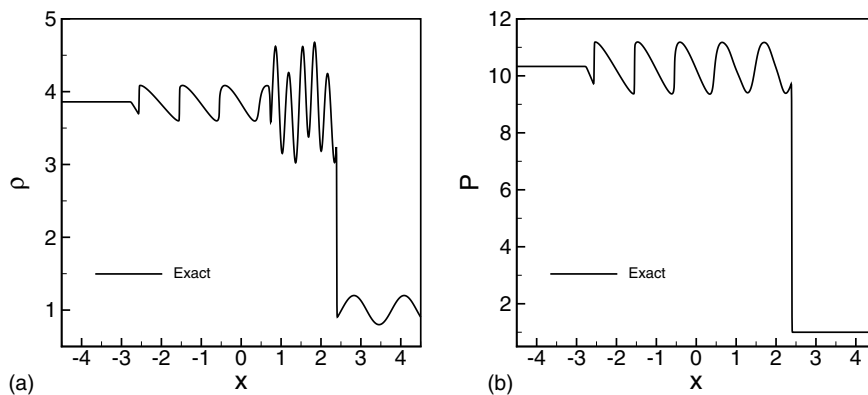


Fig. 10. Exact solution to Shu–Osher’s problem at $t = 1.8$. (a) Density and (b) pressure.

error. The density profiles for the $r = 3$ simulations are shown in Fig. 11(a) and (b) with fine and coarse grids, respectively. On the fine grid, WENO-SYM resolves the extrema. In contrast, WENO-JS is slightly damped. All WENO schemes yield damped solutions, however, the WENO-SYM solutions are less dissipative than that of the WENO-JS. While not shown, there is no difference between the behavior of the WENO-JS and WENO-SYM solutions near the shock. Similar results are found for WENO4 with slightly better predictions of the wave amplitudes.

5.4. Weak shock interacting with large-magnitude fluctuations

This test problem is similar to the Shu–Osher’s problem. However, the flow conditions are modified to consider a weak shock propagating over smooth, large-amplitude density fluctuations. The initial conditions are $u = 0.4142$, $P = 1.4018$ and $\rho = 0.6357$ for $x \geq -4$ and $u = 0$, $P = 1.0$, $\rho = 0.5 + 0.1 \sin(5x)$ for $x < 4$. This condition results in a weak shock of strength Mach 1.1 interacting with density fluctuations with magnitude of the order of 20% of the mean density. With this case, we test the efficiency of the schemes to distinguish between shocks and turbulence fluctuations. The governing equations are Eqs. (20).

As in Section 5.3, the solution is advanced to $t = 1.8$, the CFL number is 0.2, the grid is equispaced and the initial conditions are fixed at the boundaries for the duration of each simulation. The grid converged solution is used as the exact solution and is computed using the WENO-JS scheme with $r = 3$ on 400 grid points. For consistency, all schemes use $p = 2$. The exact density and pressure profiles are given in Fig. 12. Fig. 13(a) and (b) plots the density profiles for a fine grid (100 points) and a coarse grid (50 points), respectively. The results are similar to those found in Shu–Osher’s problem. On the fine grid, WENO-SYM resolves the extrema and

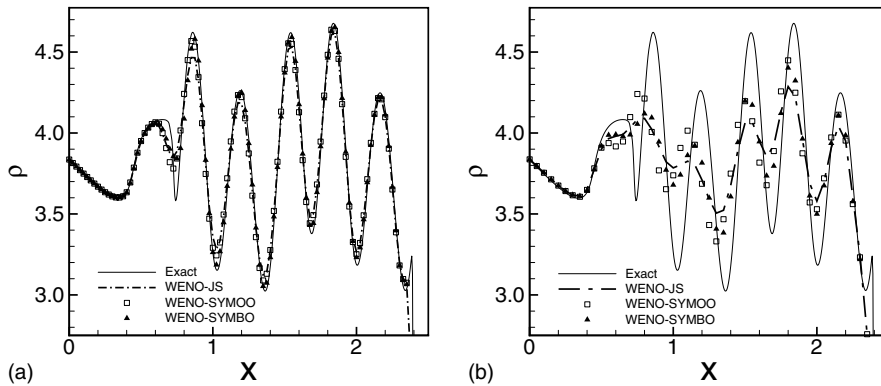


Fig. 11. Solution to Shu–Osher’s problem at $t = 1.8$ for the various WENO schemes with $r = 3$ and $p = 2$: (a) 400 and (b) 200 grid points.

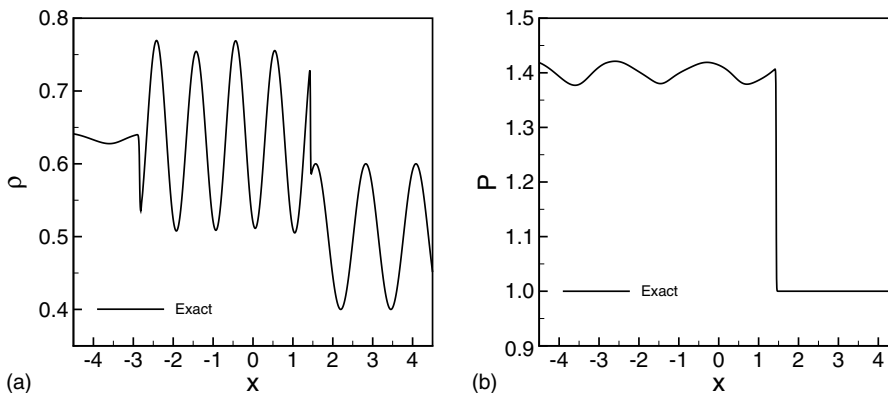


Fig. 12. Exact solution to a one-dimensional weak–shock interaction with large-magnitude fluctuations at $t = 1.8$.

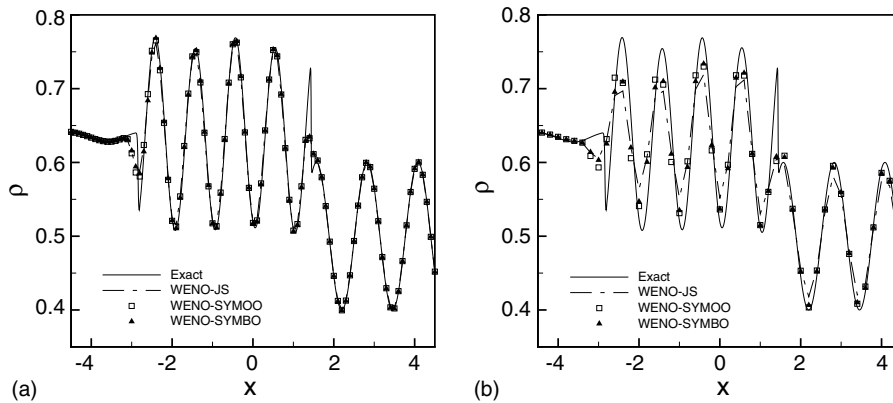


Fig. 13. Solution to a one-dimensional weak-shock interaction with large-magnitude fluctuations at $t = 1.8$ for the various WENO schemes with $r = 3$ and $p = 2$: (a) 100 and (b) 50 grid points.

WENO-JS is slightly damped. On the coarse grid all WENO yield heavily damped solutions. All schemes distinguish between the weak shock and the large-amplitude fluctuations.

5.5. Propagation of an oblique shock

In this section, we study the effect of grid-to-shock alignment by considering the Shu–Osher problem in two dimensions. Fig. 14 shows a sketch of this flow, where the shock convects at an angle θ with respect to the x -coordinate axis of the computational domain. We test two angles, $\theta = 45^\circ$ and 22° . The governing equations are Eqs. (20) and the flow conditions are those of Section 5.3. The grid is equispaced and the resolution in both directions matches that of the one-dimensional problem with 200 grid points. With this constrain, the resulting grids have 280×56 and 450×45 grid points for $\theta = 45^\circ$ and 22° , respectively.

Fig. 15(a) and (b) plots the density profiles for the oblique Shu–Osher’s problem the WENO-SYMO scheme with $r = 3$ for $\theta = 22^\circ$ and 45° , respectively. We observe no deterioration of the solution due to grid-to-shock misalignment. In fact, the solution is less dissipative for the oblique shock problem since, although the grid spacing in the x and y directions are the same as for the one-dimensional case, the grid-resolution normal to the shock direction decreases. See Fig. 14. That is the effective grid resolution in PPW is greater at $\theta = 45^\circ$.

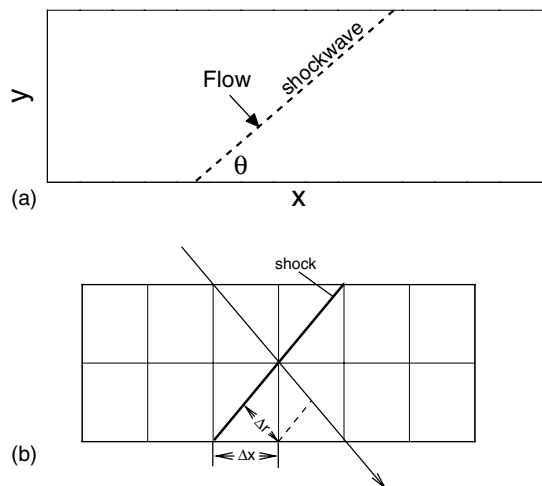


Fig. 14. Sketch of the oblique Shu–Osher’s problem.

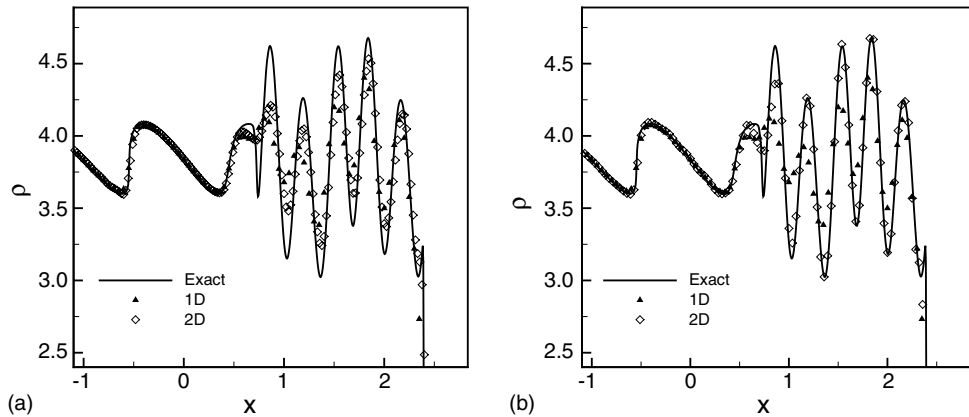


Fig. 15. Solution to the oblique Shu–Osher's problem at $t = 1.8$ for WENO-SYMBO with $r = 3$ and varying shock angle: (a) $\theta = 22^\circ$ and (b) $\theta = 45^\circ$.

6. Isotropic turbulence

Turbulence is an irregular motion that can be described by statistical values, depending on both position and time, of the quantities that characterize the flow field. When all possible states of turbulence are equally probable at any given point of the flow field, turbulence is said to be homogeneous. When turbulence is isotropic, the statistical averages are independent of the coordinate system. Isotropic, homogeneous turbulence is an idealization and its study is the simplest possible study of turbulence. In this section, we consider decaying isotropic turbulence to test the efficiency of the WENO-SYMBO methods.

The governing equations are the compressible Navier–Stokes equations.

$$\begin{aligned} \frac{\partial \rho}{\partial t} + \frac{\partial}{\partial x}(\rho u) &= 0, \\ \frac{\partial(\rho u)}{\partial t} + \frac{\partial}{\partial x}(\rho u^2 + P - \sigma_{ij}) &= 0, \\ \frac{\partial E}{\partial t} + \frac{\partial}{\partial x}[(E + P)u + q_j - u_i \sigma_{ij}] &= 0, \end{aligned} \quad (20)$$

where σ is the shear stress tensor given by a linear stress–strain relationship

$$\sigma_{ij} = \mu \left(\frac{\partial u_i}{\partial x_j} + \frac{\partial u_j}{\partial x_i} \right) - \frac{2}{3} \mu \frac{\partial u_k}{\partial x_k} \delta_{ij}, \quad (21)$$

where μ is the viscosity, which is given by $\mu = \mu_{\text{ref}} \left(\frac{T}{T_{\text{ref}}} \right)^n$ with the reference values μ_{ref} and T_{ref} taken for air at atmospheric conditions; and q_j is the heat flux given by

$$q_j = -\kappa \frac{\partial T}{\partial x_j}, \quad (22)$$

where κ is the thermal diffusivity, which is related to the gas viscosity by $\kappa = 3.5\mu R$ for air.

The governing parameters for decaying isotropic turbulence are the turbulent Mach number $M_t = q/a$ and the Reynolds number based on the Taylor microscale $Re_\lambda = \rho u_{\text{RMS}} \lambda / \mu$, where $q = \langle u_i u_i \rangle$, $\langle \cdot \rangle$ indicates an ensemble average, u_i is the velocity in the i th direction, λ is the Taylor microscale and u_{RMS} is the root-mean-squared of the velocity in one direction.

We first consider nearly incompressible flow conditions where shockwaves are not present and the comparison against a sixth-order accurate Padé scheme is meaningful. The initial flow conditions are $M_t = 0.1$ and $Re_\lambda = 35$, and the grids are equispaced. We simulate the decay of isotropic turbulence for one non-dimensional time period based on the initial large-eddy turn over time, $\tau_t = \lambda / u_{\text{RMS}}$. The length of the simulation and the simulation parameters are representative of those used to study fundamental physical phenomena

or develop turbulence models in isotropic turbulence [20–22]. Fig. 16(a) shows the temporal evolution of turbulent kinetic energy for the Padé and WENO methods with $r = 3$ on meshes with 64^3 and 128^3 grid points. scheme gives grid converged results with 64^3 grid points, whereas the WENO schemes are more dissipative and require 128^3 . Fig. 16(b) shows the energy spectra at $\tau_t = 1.0$ for the same simulations. Aliasing errors are found for the WENO scheme with 128^3 grid points in the tail of the spectrum, which does not affect the results. than WENO-JS. Similar results are found for $r = 4$ in Fig. 17.

We now consider a shock-containing simulation with initial conditions $M_t = 1.5$ and $Re_\lambda = 50$. For this Reynolds number case, 192^3 grid points are required to obtain grid-converged results, where convergence is achieved in the sense that the temporal decay of turbulent kinetic energy and the distribution of energy in frequency space do not change as the resolution is further decreased. In addition, Re_λ is high enough so that the data exhibit an inertial range. Fig. 18(a) shows the energy spectra at $\tau_t = 1.5$. We observe that the spectrum exhibits the inertial range with slope $k^{-5/3}$, showing the accuracy of the data. Fig. 18(b) shows contours of density on a two-dimensional plane. The steep gradients show the location of shockwaves.

As reference, we can compute the ratio of the average shock thickness to the smallest turbulence length scale in the flow. The shock thickness is of the order of the molecular mean free path, l . The smallest length scale is given by the Kolmogorov length scale, η . These are given by

$$l = \frac{\mu}{\rho} \sqrt{\frac{\pi}{2} \frac{1}{RT}}, \tag{23}$$

$$\eta = \lambda 15^{-0.25} Re_\lambda^{-0.5}.$$

In turn l/η is about 0.42. To determine the numerical shock width, λ_s , we use a shock-detection algorithm [23]. The numerical approximation gives $\lambda_s/\eta = 6.25$.

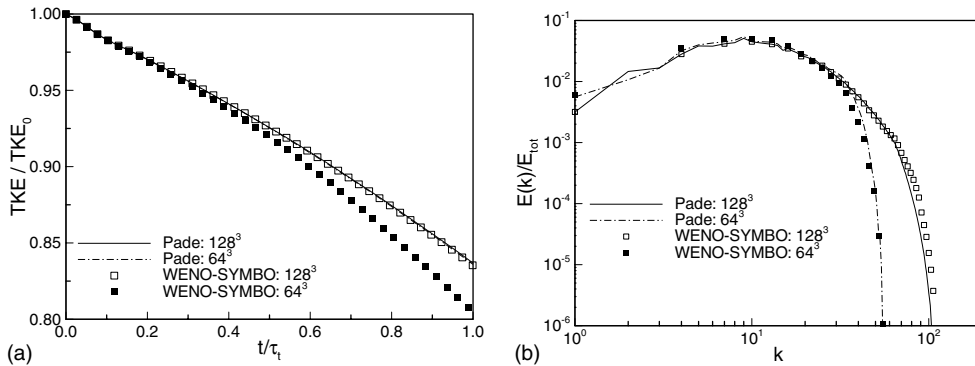


Fig. 16. DNS data of decaying isotropic turbulence at $M_t = 0.1$ and $Re_\lambda = 35$, comparing the WENO with $r = 3$ and Padé schemes. (a) Temporal evolution of turbulent kinetic energy and (b) energy spectra at $\tau_t = 1.0$.

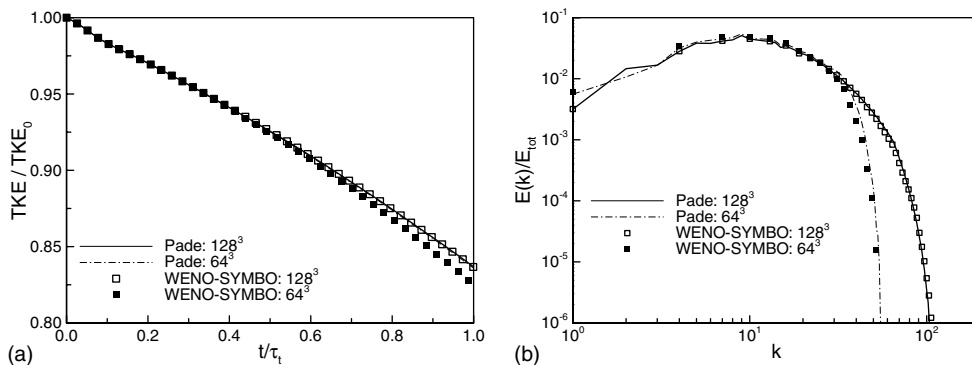


Fig. 17. DNS data of decaying isotropic turbulence at $M_t = 0.1$ and $Re_\lambda = 35$, comparing the WENO with $r = 4$ and Padé schemes. (a) Temporal evolution of turbulent kinetic energy and (b) energy spectra at $\tau_t = 1.0$.

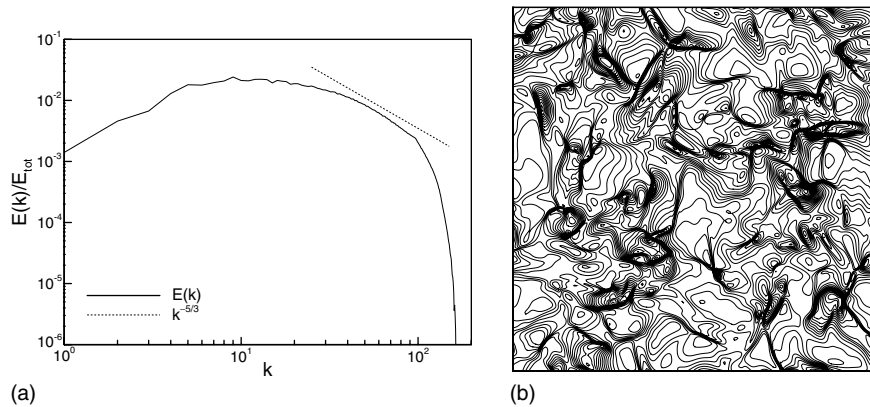


Fig. 18. (a) Energy spectrum and (b) density contours from the DNS data of decaying isotropic turbulence with $M_t = 1.5$ and $Re_\lambda = 50$ at $t/\tau_t = 1.5$ using the bandwidth-optimized WENO scheme.

7. Compressible turbulent boundary layer

Simulations of turbulent boundary layers are computationally expensive. Thus, we consider only the results given by the bandwidth-optimized WENO scheme, WENO-SYMO, with $r = 3$. This scheme has a narrower stencil than $r = 4$ and it is therefore less expensive on a given grid. The governing equation is Eq. (21).

We consider the experimental conditions of Debiève [24–26] with $M = 2.32$, Reynolds number based on the momentum thickness $Re_\theta = 4000$ and Elena [27,28] with $M = 2.32$ and $Re_\theta = 4700$. The number of grid points and domain size are $328 \times 256 \times 120$ and $7.1\delta \times 2.1\delta \times 16.6\delta$ in the streamwise, spanwise and wall-normal directions, respectively. The initial conditions are those of Martín [29] and we use rescaling boundary conditions [30] to provide the inflow. Thus, we simulate a fixed spatial location of a spatially developing boundary layer and Re_θ is about 4600. We gather statistics for 70 non-dimensional time periods $\tau_t = \delta^*/U_e$, where δ^* is the displacement thickness and U_e is the velocity at the boundary layer edge. The spacing between fields is about $1.5 \tau_t$. The results are validated against the experimental data.

Fig. 19 plots the mean flow profiles for the DNS and experimental data. Fig. 20(a) and (b) plots the normalized magnitude of velocity and temperature fluctuations, respectively, in comparison with the experiments

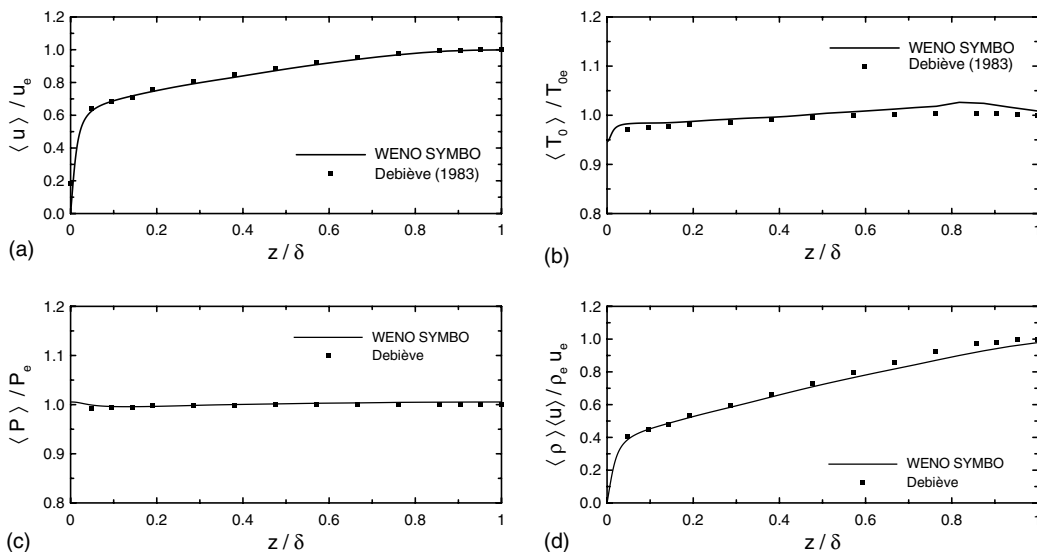


Fig. 19. Comparison between DNS using the bandwidth-optimized WENO scheme at $M = 2.32$ and $Re_\theta = 4450$ and experimental data (Refs. [24–26]). Normalized values of mean (a) velocity; (b) total temperature; (c) pressure; (d) momentum. Quantities are normalized using edge values.

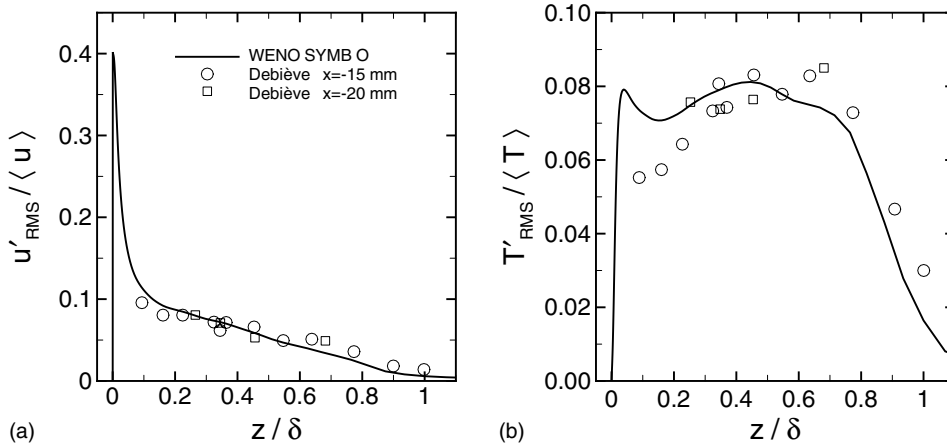


Fig. 20. Comparison between DNS using the bandwidth-optimized WENO scheme at $M = 2.32$ and $Re_\theta = 4450$ and experimental data (Refs. [24–26]). (a) Streamwise component of turbulent fluctuations; (b) Turbulent temperature fluctuations. Quantities are normalized using mean flow variables.

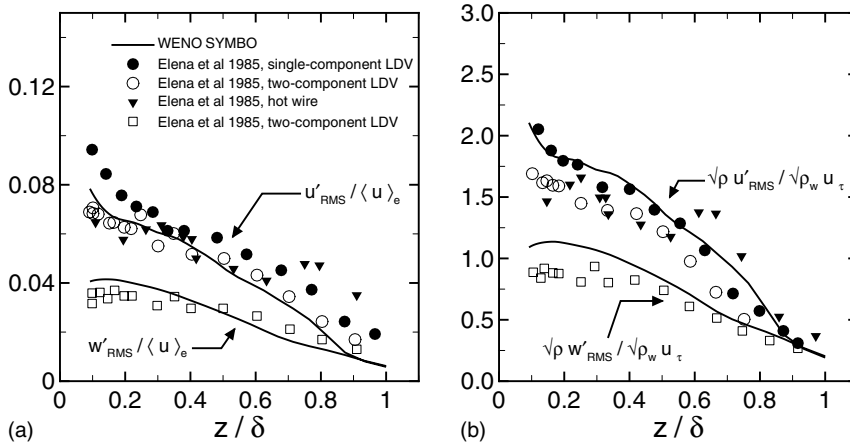


Fig. 21. RK3 and DP2 simulations of a turbulent boundary layer with $CFL = 1$ and comparison with experimental data [27,28]. (a) Magnitude of velocity fluctuations normalized with edge velocity; (b) magnitude of velocity fluctuations normalized with Morkovin's scaling.

of Debiève, and Fig. 21(a) and (b) shows the magnitude of the streamwise and wall-normal velocity fluctuations in comparison to the experiments of Elena, where the data are normalized using the edge and friction velocities respectively. The criterion for good accuracy is that the simulation data agrees with the experimental data to within the scatter of the experimental data. It should be noted that accessing the near-wall region ($z/\delta \leq 0.2$) is not possible experimentally. Thus, the experimental data are not accurate very close to the wall. The DNS data are within the scatter of the experimental data.

8. Conclusions

We present two formulations of a symmetric WENO method for the simulation of turbulent compressible flows. The new methods are based on the scheme of Jiang and Shu [8] and are optimized to maximize order of accuracy and bandwidth while minimizing dissipation. Third-order- and fourth-order-accurate formulations are considered. The accuracy of the methods is assessed for canonical problems such as shock tube flow, Shu–Osher's problem, oblique Shu–Osher's problem, weak shockwave propagating into large-amplitude smooth density fluctuations and the propagation of smooth fluctuations. It is found that the order-optimized

scheme WENO-SYMOO can result in instabilities near contact surfaces. The results from the canonical flow simulations also show that the bandwidth-optimized schemes are less dissipative than the original WENO-JS.

Direct numerical simulations of turbulent flows are also considered. It is shown that both schemes give accurate turbulence results. Incompressible simulations of decaying isotropic turbulence show good agreement between WENO-SYMOO and the sixth-order-accurate, central Padé scheme. In addition, WENO-SYMOO can be used to simulate higher turbulent Mach number isotropic turbulence with DNS. Data at $M_t = 1.5$ show accurate frequency distribution of turbulent kinetic energy with a $k^{-5/3}$ inertial range, and the flow field exhibits an abundant number of shockwaves. Finally, the DNS data of a supersonic boundary layer simulated with a WENO-SYMOO scheme shows good agreement with experimental data.

Majda and Osher [31] show that when shocks are involved, numerical methods lose formal order of accuracy. It has also been shown [32,33] that the convergence rate reduces to first order at a discontinuity, and first order errors at the shock propagate out into the post-shock region by following characteristics that emerge at the shock [34]. The solution error can be characterized by a high-order component and a first-order component, which is nearly independent of the designed numerical error [35]. For smooth flows, the solution is formally high-order accurate. Whereas for flows containing under-resolved shocks, the solution is no longer formally high-order accurate. Thus, those portions of the domain where information propagates through the shock are subject to the shock-capturing error. This issue is endemic to all shock-capturing methodologies, including hybrid methods. In the present simulations of compressible turbulence, the shock-capturing error is considered acceptable.

The benefit of WENO methods is robust shock capturing. So far, the limitation for these methods is the slow grid convergence. In the present manuscript, we have addressed the reduction of phase and dissipation errors in the linear part of the scheme. Further optimization of the non-linear part might lead to improved grid convergence and is the subject of future work.

Acknowledgments

This work was sponsored in part by the National Science Foundation under Grant number CTS-0238390 and by the Air Force Office of Scientific Research grant AF/F49620-02-1-0361. The computing time was provided by the CROCCO Laboratory in Princeton University.

Appendix

This appendix presents the weights and coefficients for the WENO-JS, WENO-SYMOO and WENO-SYMO schemes (see Tables 1–7).

Table 1
Candidate flux stencil coefficients a_{ki}^3 for both WENO-JS and WENO-SYM

	$l = 0$	$l = 1$	$l = 2$
$k = 0$	2/6	−7/6	11/6
$k = 1$	−1/6	5/6	2/6
$k = 2$	2/6	5/6	−1/6
$k = 3$	11/6	−7/6	2/6

Note that $k = 3$ is relevant only for the latter.

Table 2
Candidate flux stencil coefficients a_{ki}^4 for both WENO-JS and WENO-SYM

	$l = 0$	$l = 1$	$l = 2$	$l = 3$
$k = 0$	−6/24	26/24	−46/24	50/24
$k = 1$	2/24	−10/24	26/24	6/24
$k = 2$	−2/24	14/24	14/24	−2/24
$k = 3$	6/24	26/24	−10/24	2/24
$k = 4$	50/24	−46/24	26/24	−6/24

Note that $k = 4$ is relevant only for the latter.

Table 3
Smoothness measurement stencil coefficients d_{kml}^3 for both WENO-JS and WENO-SYM

	$m = 1$		
	$l = 0$	$l = 1$	$l = 2$
$k = 0$	1/2	-4/2	3/2
$k = 1$	-1/2	0	1/2
$k = 2$	-3/2	4/2	-1/2
$k = 3$	-5/2	8/2	-3/2
	$m = 2$		
	$l = 0$	$l = 1$	$l = 2$
$k = 0$	β_2	$-2\beta_2$	β_2
$k = 1$	β_2	$-2\beta_2$	β_2
$k = 2$	β_2	$-2\beta_2$	β_2
$k = 3$	β_2	$-2\beta_2$	β_2

Note that $k = 3$ is relevant only for the latter. $\beta_2 = \sqrt{13/12}$.

Table 4
Smoothness measurement stencil coefficients d_{kml}^4 for both WENO-JS and WENO-SYM

	$m = 1$			
	$l = 0$	$l = 1$	$l = 2$	$l = 3$
$k = 0$	-2/6	9/6	-18/6	11/6
$k = 1$	1/6	-6/6	3/6	2/6
$k = 2$	-2/6	-3/6	6/6	-1/6
$k = 3$	-11/6	18/6	-9/6	2/6
$k = 4$	-26/6	57/6	-42/6	11/6
	$m = 2$			
	$l = 0$	$l = 1$	$l = 2$	$l = 3$
$k = 0$	$-\beta_2$	$4\beta_2$	$-5\beta_2$	$2\beta_2$
$k = 1$	0	β_2	$-2\beta_2$	β_2
$k = 2$	β_2	$-2\beta_2$	β_2	0
$k = 3$	$2\beta_2$	$-5\beta_2$	$4\beta_2$	$-\beta_2$
$k = 4$	$3\beta_2$	$-8\beta_2$	$7\beta_2$	$-2\beta_2$
	$m = 3$			
	$l = 0$	$l = 1$	$l = 2$	$l = 3$
$k = 0$	$-\beta_3$	$3\beta_3$	$-3\beta_3$	β_3
$k = 1$	$-\beta_3$	$3\beta_3$	$-3\beta_3$	β_3
$k = 2$	$-\beta_3$	$3\beta_3$	$-3\beta_3$	β_3
$k = 3$	$-\beta_3$	$3\beta_3$	$-3\beta_3$	β_3
$k = 4$	$-\beta_3$	$3\beta_3$	$-3\beta_3$	β_3

Note that $k = 4$ is relevant only for the latter. $\beta_2 = \sqrt{13/12}$ and $\beta_3 = \sqrt{781/720}$.

Table 5
Order-optimized optimal weights C_k^r for WENO-JS when $r = 3$ and $r = 4$

k	C_k^3	C_k^4
0	1/10	1/35
1	6/10	12/35
2	3/10	18/35
3	N/A	4/35

Table 6

Order-optimized optimal weights \bar{C}_k^r for WENO-SYMOO when $r = 3$ and $r = 4$

k	\bar{C}_k^3	\bar{C}_k^4
0	1/20	1/70
1	9/20	16/70
2	9/20	36/70
3	1/20	16/70
4	N/A	1/70

Table 7

Bandwidth-optimized optimal weights \tilde{C}_k^r for WENO-SYMOO when $r = 3$ and $r = 4$

k	\tilde{C}_k^3	\tilde{C}_k^4
0	0.094647545896	0.040195483373
1	0.428074212384	0.249380000671
2	0.408289331408	0.480268625626
3	0.068988910311	0.200977547673
4	N/A	0.029178342658

References

- [1] M.P. Martín, Shock capturing in LES of high-speed flows, Annual Research Briefs of the Center for Turbulence Research, Stanford University, 2000, pp. 193–198.
- [2] R. Samtaney, D.I. Pullin, B. Kosovic, Direct numerical simulation of decaying compressible turbulence and shocklet statistics, *Physics of Fluids* 13 (2001) 1415–1430.
- [3] M. Wu, P. Bookey, M.P. Martín, A.J. Smits, Analysis of shockwave/turbulent boundary layer interaction using DNS and experimental data, AIAA Paper No. 2005-0310, 2005.
- [4] M. Wu, E.M. Taylor, M.P. Martín, Assessment of STBLI DNS data and comparison against experiments, AIAA Paper No. 2005-4895, 2005.
- [5] X.-D. Liu, S. Osher, T. Chan, Weighted essentially non-oscillatory schemes, *Journal of Computational Physics* 115 (1994) 200–212.
- [6] C.-W. Shu, S. Osher, Efficient implementation of essentially non-oscillatory shock capturing schemes, *Journal of Computational Physics* 77 (1988) 439–471.
- [7] C.-W. Shu, S. Osher, Efficient implementation of essentially non-oscillatory shock-capturing schemes, ii, *Journal of Computational Physics* 83 (1989) 32–78.
- [8] G.-S. Jiang, C.-W. Shu, Efficient implementation of weighted ENO schemes, *Journal of Computational Physics* 126 (1) (1996) 202–228.
- [9] N.A. Adams, K. Shariff, A high-resolution hybrid compact ENO scheme for shock-turbulence interaction problems, *Journal of Computational Physics* 127 (1996) 27.
- [10] S. Pirozzoli, Conservative hybrid compact-weno schemes for shock-turbulence interaction, *Journal of Computational Physics* 178 (2002) 81–117.
- [11] Y.-X. Ren, M. Liu, H. Zhang, A characteristic-wise compact-WENO scheme for solving hyperbolic conservation laws, *Journal of Computational Physics* 192 (2003) 365–386.
- [12] D.J. Hill, D.I. Pullin, Hybrid tuned center-difference-WENO method for large-eddy simulation in the presence of strong shocks, *Journal of Computational Physics* 194 (2004) 435–450.
- [13] D. Kim, J.H. Kwon, A high-order accurate hybrid scheme using a central flux scheme and a WENO scheme for compressible flowfield analysis, *Journal of Computational Physics* 215 (2) (2006) 417–429.
- [14] Z.J. Wang, R.F. Chen, Optimized weighted essentially nonoscillatory schemes for linear waves with discontinuity, *Journal of Computational Physics* 174 (2001) 381–404.
- [15] S.K. Lele, Compact finite-difference schemes with spectral-like resolution, *Journal of Computational Physics* 103 (1) (1992) 16–42.
- [16] V.G. Weirs, A numerical method for the direct simulation of compressible turbulence. PhD Thesis, University of Minnesota (also AIAA Paper 1997-1940 with corrections), December, 1998.
- [17] C.K.W. Tam, J.C. Webb, Dispersion-relation-preserving finite difference schemes for computational acoustics, *Journal of Computational Physics* 107 (1993) 262–281.
- [18] D.P. Lockhard, K.S. Brentner, H.L. Atkins, High-accuracy algorithms for computational aeroacoustics, *AIAA Journal* 32 (2) (1995) 246–251.
- [19] S. Wolfram, *The Mathematica Book*, fifth ed., Wolfram Media, 2003.
- [20] S. Lee, S.K. Lele, P. Moin, Eddy-shocklets in decaying compressible turbulence, *Physics of Fluids* 3 (1991) 657.
- [21] M.P. Martín, G.V. Candler, Effect of chemical reactions on decaying isotropic turbulence, *Physics of Fluids* 10 (1998) 1715.

- [22] M.P. Martín, U. Piomelli, G.V. Candler, Subgrid-scale models for compressible large-eddy simulations, *Theoretical and Computational Fluid Dynamics* 13 (2000) 361–376.
- [23] E.M. Taylor, M.P. Martín, Stencil adaptation properties of a WENO scheme in direct numerical simulations of compressible turbulence, *Journal of Scientific Computing*, accepted for publication. Also in AIAA Paper No. 2004-2706, 2004.
- [24] J.F. Debiève, H. Gouin, J. Gaviglio, Momentum and temperature fluxes in a shock wave–turbulence interaction, in: *Proceedings ICHMT/IUTAM Symposium on the Structure of Turbulence and Heat and Mass Transfer*, Dubrovnik, 1981.
- [25] J.F. Debiève, Etude d’une interaction turbulence onde de choc, PhD Thesis, Thèse Université d’Aix Marseille II, Marseille, France, 1983.
- [26] H.H. Fernholz, P.J. Finley, J.P. Dussauge, A.J. Smits, A survey of measurements and measuring techniques in rapidly distorted compressible turbulent boundary layers, *AGARDograph* (1989) 315.
- [27] M. Eléna, J.P. Lacharme, J. Gaviglio, Comparison of hot-wire and laser Doppler anemometry methods in supersonic turbulent boundary layers, *ASME*, 1985.
- [28] M. Eléna, J.P. Lacharme, Experimental study of a supersonic turbulent boundary layer using a laser Doppler anemometer, *Journal Mécanique Théorique et Appliquée* 7 (1988) 175.
- [29] M.P. Martín, DNS of hypersonic turbulent boundary layers. Part I: Initialization and comparison with experiments, *Journal of Fluid Mechanics*, accepted for publication.
- [30] S. Xu, M.P. Martín, Assessment of inflow boundary conditions for compressible turbulent boundary layers, *Physics of Fluids* 16 (7) (2004). Also AIAA Paper No. 2003-3963, June, 2003.
- [31] A. Majda, S. Osher, Propagation of error into regions of smoothness for accurate difference approximations to hyperbolic equations, *Communications on Pure and Applied Mathematics* 30 (6) (1977) 671–705.
- [32] J. Casper, M.H. Carpenter, Computational considerations for the simulation of shock-induced sound, *SIAM Journal of Scientific Computing* 19 (1998) 813–828.
- [33] J.A. Greenough, W.J. Rider, A quantitative comparison of numerical methods for the compressible Euler equations: fifth-order weno piecewise-linear godunov, *Journal of Computational Physics* 196 (2004) 259–281.
- [34] B. Engquist, B. Sjögreen, The convergence rate of finite difference schemes in the presence of shocks, *SIAM Journal of Numerical Analysis* 35 (1998) 2464–2485.
- [35] M.H. Carpenter, J.H. Casper, Accuracy of shock capturing in two spatial dimensions, *AIAA Journal* 37 (1999) 1072–1079.